Soluble surfactant spreading on spatially confined thin liquid films

Soft Matter c2sm25484k

PAPER

1

Soluble surfactant spreading on spatially confined thin liquid films

Myroslava Hanyak, David K. N. Sinz and Anton A. Darhuber

We elucidate the influence of confinement induced by chemical patterning on the spreading of soluble surfactants along thin liquid films.

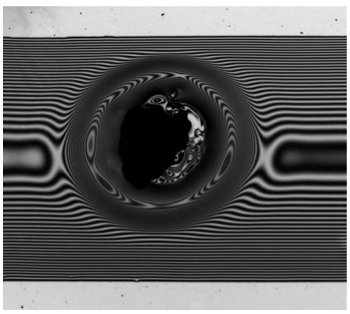

Please check this proof carefully. **Our staff will not read it in detail after you have returned it**.

Translation errors between word-processor files and typesetting systems can occur so the whole proof needs to be read. Please pay particular attention to: tabulated material; equations; numerical data; figures and graphics; and references. If you have not already indicated the corresponding author(s) please mark their name(s) with an asterisk. Please e-mail a list of corrections or the PDF with electronic notes attached – do not change the text within the PDF file or send a revised manuscript.

Please bear in mind that minor layout improvements, e.g. in line breaking, table widths and graphic placement, are routinely applied to the final version.

We will publish articles on the web as soon as possible after receiving your corrections; no late corrections will be made.

Please return your **final** corrections, where possible within **48 hours** of receipt by e-mail to: softmatter@rsc.org

Reprints—Electronic (PDF) reprints will be provided free of charge to the corresponding author. Enquiries about purchasing paper reprints should be addressed via: http://www.rsc.org/publishing/journals/guidelines/paperreprints/. Costs for reprints are below:

Reprint costs

No of pages	Cost (per 50 copies)	
	First	Each additional
2–4	£225	£125
5–8	£350	£240
9–20	£675	£550
21–40	£1250	£975
>40	£1850	£1550

Cost for including cover of journal issue:
£55 per 50 copies

Soft Matter

Dynamic Article Links

Cite this: DOI: 10.1039/c2sm25484k

www.rsc.org/softmatter

PAPER

Soluble surfactant spreading on spatially confined thin liquid films

Myroslava Hanyak, David K. N. Sinz and Anton A. Darhuber

Received 1st March 2012, Accepted 29th May 2012
DOI: 10.1039/c2sm25484k

We studied the spreading of soluble surfactants on spatially confined thin liquid films by means of comprehensive experiments and numerical simulations. We determined the time evolution of the liquid film thickness both from interference microscopy measurements and finite element calculations. A characteristic rim develops ahead of the spreading surfactant front. Within certain time intervals, the rim position can be well represented by a power-law relation $x_{\mathrm{rim}} \approx t^{\alpha}$. The corresponding spreading exponent α depends on the method of surfactant deposition and the numerical values deduced from experiments and simulations quantitatively agree. Depth-resolved simulations that account for domain deformability using the Arbitrary Lagrangian–Eulerian method show that shear-induced concentration non-uniformities across the rim film thickness tend to reduce the rim height. Fingering instabilities that are frequently observed in experiments were qualitatively reproduced in the simulations.

I. Introduction

In the context of oil recovery, up to about 60% of the originally present crude oil remains in a reservoir after the primary and secondary recovery phases.[27,28] Injection of surfactant solutions is considered a potential means for extracting more oil from subsurface oil reservoirs.[41,44] Non-uniform surfactant distributions at fluid–fluid interfaces give rise to interfacial tension gradients and associated Marangoni stresses, which locally cause flow from regions of lower to regions of higher interfacial tension.

The spreading of insoluble surfactants at the air–liquid interface of thin liquid films has been extensively studied.[3,7,8,15–17,19,20,25,26,33,34,36,45,46,48,51,53] It was observed that film thinning occurred in the vicinity of the deposited surfactant as well as film thickening and the formation of a rim near the surfactant leading edge. The rim position $x_{\mathrm{rim}}(t)$ follows a power law behavior $x_{\mathrm{rim}} \approx t^{\alpha}$, where α is the so-called spreading exponent. A variety of spreading exponents were reported for different material systems and geometrical configurations: $\alpha = 0.5$ for planar spreading,[3,7] exponents around $\alpha = 0.25$ for axisymmetric spreading with large Peclet numbers[19,20] and values around 0.33 for spreading along chemically defined liquid rivulets.[45]

In technological applications, surfactants are often soluble in at least one phase. The spreading dynamics of soluble surfactants at air–liquid and liquid–liquid interfaces has been studied in ref. 1,2,4,5,10,21,24,29,30,32,35,36,39,50 and 54. Troian *et al.* reported the occurrence of a fingering instability at the spreading edge of the surfactant droplet deposited on a thin liquid film.[50] The growth rate of the fingers was measured to be 0.7 and 0.66 for thick and thin films, respectively. Jensen and Grotberg presented a one-dimensional model for the spreading of soluble surfactants[24] considering linearized Langmuir sorption kinetics and fast vertical diffusion across the film thickness. Different solubilities of the surfactant induced qualitative differences in the flow patterns. Lin *et al.* pointed out that the generalized Frumkin model for the surfactant adsorption–desorption dynamics resulted in a higher spreading rate as compared to the Langmuir model.[32] Craster and Matar[10] considered wettability modification due to surfactant adsorption at liquid–solid interfaces. Berg[5] performed surfactant spreading experiments along a flat interface between deep, immiscible fluid layers and observed spreading exponents equal to $\alpha = 3/4$.

In the context of pulmonary surfactant transport, several groups investigated exogenous surfactant spreading along thin liquid films adhering to the interior surface of hollow tubes.[12,14,18,52,56] Espinosa *et al.*[14] found that the effect of circumferential curvature was negligible, as if spreading occurred over a flat surface. For a linear equation of state, a spreading exponent $\alpha = 1/3$ was reported. Williams and Jensen[56] considered the effect of circumferential non-uniformities of the liquid film thickness and concluded that flow-induced shape deformations of the liquid lining influence the spreading dynamics only weakly.

Numerical methods for interfacial flows involving insoluble surfactants include the volume-of-fluid scheme used to describe axisymmetric spreading of the surfactant on a moving liquid–fluid interface[23] and the level-set method applied for two-dimensional spreading.[58] For the computationally more challenging flows with soluble surfactants, a diffuse interface method was presented by Van der Smaan and Van der Graaf[47] for surfactant adsorption onto liquid interfaces. A diffuse-interface implementation including the effects of advection, diffusion and

Mesoscopic Transport Phenomena Group, Department of Applied Physics, Eindhoven University of Technology, Postbus 513, 5600MB Eindhoven, The Netherlands

bulk–surface exchange of soluble surfactants was introduced by Teigen *et al.*[49] together with a finite difference technique to model two-phase flows. Their approach was limited to relatively low Peclet numbers. High Peclet numbers pose a computational challenge due to the occurrence of concentration boundary layers. Recently, Booty and Siegel presented a hybrid numerical method incorporating a perturbation analysis of the layer and a full numerical solution of boundary problem.[6]

In this manuscript, we systematically study the spreading of soluble surfactants along thin liquid films deposited on chemically patterned surfaces using both experiments and numerical simulations. Completely and partially wetting patterns confine the location and flow of liquid to predefined regions on the substrate in the shape of long and narrow stripes. We investigate the consequences of geometrical confinement and the non-zero curvature of the interface on the surfactant spreading dynamics as a first step towards more complex, branched and three-dimensional geometries encountered in porous media.

Since the aspect ratio of the thin liquid films is very small, we apply the lubrication approximation[24,38] for the description of the spreading dynamics and achieve excellent agreement with the spreading exponents observed in interference microscopy experiments. The underlying assumption of a vertically uniform concentration distribution is strictly valid only for sufficiently large diffusion coefficients or sufficiently small film thicknesses, *i.e.* sufficiently small Peclet numbers Pe. For large Pe we apply a finite-element-based Navier–Stokes solver used in conjunction with an arbitrary Lagrangian–Eulerian technique to model soluble surfactant spreading and account for the domain deformability. This novel scheme allows for values of the Peclet number up to approximately 10^5, based on the velocity scale of Marangoni spreading.

In Section II we describe the sample fabrication, the experimental setup and procedures. Typical experimental results are presented in Section III. In Section IV we outline the theoretical model for the spreading dynamics of soluble surfactants on thin liquid films along with its numerical implementation. Numerical results are presented in Section V, followed by a comparison with experimental data in Section VI.

II. Experimental procedure

Single-side polished Silicon wafers (n-type doped with P) with a diameter of 150 mm obtained from Silicon Quest (batch number SQ13869) were cut to dimensions of typically 50 mm × 50 mm × 0.7 mm. The substrates were cleaned in two steps, first by immersion in a solution of hydrogen peroxide (30%, J.T. Baker product number 7047) and sulfuric acid (95%, J.T. Baker product number 6057), mixed at a volume ratio of 1 : 1, and subsequently by exposure to an oxygen plasma. Self-assembled monolayers of 1*H*,1*H*,2*H*,2*H*-perfluorooctyl-trichlorosilane (PFOTS, purity >97%, Sigma-Aldrich product number 448931) were used to fabricate chemical surface patterns. The patterns were created by vapor deposition of PFOTS in a sealed glass jar at $T = 100$ °C onto photolithographically masked substrates, *i.e.* the hydrophilic regions were covered with photo-resist and the partially wetting ones were left uncovered prior to the vapor deposition. Rectangular shaped hydrophilic patterns were used in the experiments described here. The width of the hydrophilic patterns was $w \leq 1.5$ mm and the length was $L = 40$–70 mm. The advancing contact angle for glycerol was between 70° and 90° on the partially wetting and 0° on the hydrophilic areas with sufficient spatial uniformity, which is essential for the reproducibility of the measurements.

Using the aforementioned mixture of hydrogen peroxide and sulfuric acid, the hydrophilic regions were repeatedly cleaned prior to each experiment. Following the cleaning, liquid films (rivulets) of anhydrous glycerol (Sigma-Aldrich product number 49767, purity 99%), with density $\rho = 1.26$ g cm^{-3} and surface tension $\gamma = 63.4$ mN m^{-1},[37] were spin-coated onto the hydrophilic regions, resulting in a center thickness in the range of $h_0 = 1$–10 μm. Fig. 1(a) shows a typical example of a rivulet prior to surfactant deposition. We conducted our experiments at a temperature of 25 °C and determined the associated viscosity of glycerol as μ (25 °C) = (876 ± 3) mPa s using a Brookfield DV-II+ Pro viscometer which agrees with literature values[31,43] for pure glycerol.

The soluble surfactant sodium dodecyl sulfate (SDS, Sigma-Aldrich product number 436143, purity 99%) is a surface-active substance that is soluble in glycerol. We determined the dependence of the glycerol surface tension γ on the SDS bulk concentration c experimentally using a Wilhelmy plate technique, with the resulting data shown in Fig. 2. For concentrations c exceeding 0.064 mol l^{-1}, a pronounced kink is visible in Fig. 2, which we ascribe to the formation of micelles. In this range we furthermore observed gelation of the liquid associated with a strong change in the rheology of the liquid which made surface tension determination in this concentration region somewhat unreliable. We were unable to find literature values for

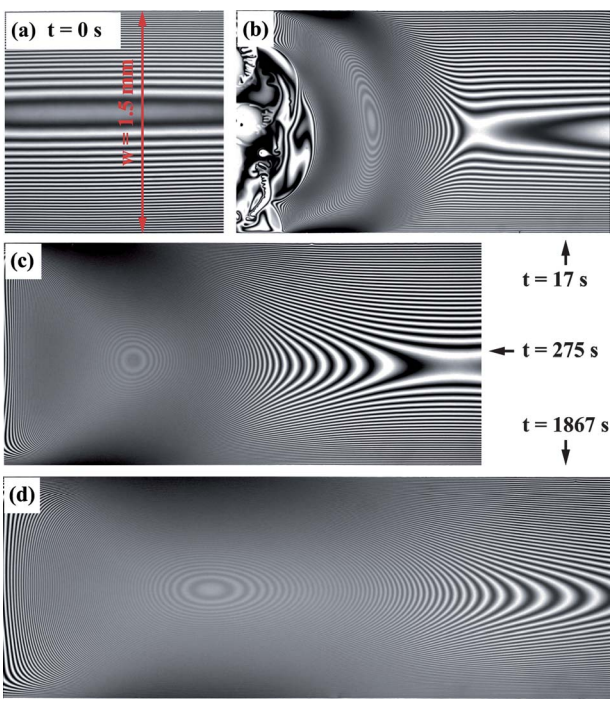

Fig. 1 Interference microscopy images of a glycerol rivulet, (a) prior to surfactant deposition at $t = 0$, as well as after deposition of compressed SDS powder, (b) $t = 17$ s, (c) $t = 275$ s and (d) $t = 1867$ s. Rivulet width $w = 1.5$ mm and initial center height $h_0 = 5.63$ μm.

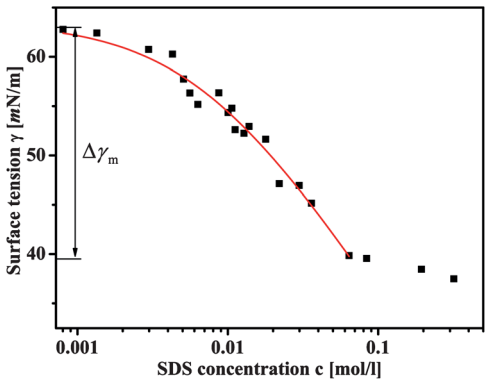

Fig. 2 Surface tension of glycerol as a function of the SDS bulk concentration.

the bulk diffusion coefficient D_b of SDS in glycerol. We estimate the value of D_b as (2–5) $\times$ 10^{-13} m^2 s^{-1} based on the measurements for SDS in water,[55] the viscosity ratio and the Stokes–Einstein relation.

We conducted two types of experiments to investigate the spreading dynamics of SDS on glycerol rivulets. In the first type termed *solution deposition*, a 0.1–0.2 μl droplet of an SDS–glycerol solution was deposited onto the sub-phase film. In the second type termed *solid deposition*, a small pellet of compressed SDS powder was deposited. Fig. 1 shows a series of exemplary interference microscopy images obtained for a rivulet of width $w = 1.5$ mm and solid deposition.

The dynamics following surfactant deposition were monitored by means of interference microscopy using an Olympus BX51 upright microscope. Depending on the sub-phase film height, the illuminating light was passband-limited around a center wavelength of $\lambda = 750$ nm or $\lambda = 550$ nm with a bandpass of $\Delta\lambda \approx 10$ nm providing a resolution of 10–20 nm. All experiments have been performed in a horizontal orientation with the liquid deposited on the upper side of the substrates.

III. Experimental results

The deposited surfactant dissolves into the underlying sub-phase liquid and locally reduces its surface tension inducing Marangoni stresses that in the case of thin liquid films cause a net flow away from the deposition region. A local maximum in the height profile is visible in Fig. 1(b–d), which is propagating along the rivulet. In the immediate vicinity of the deposited surfactant pellet, pronounced film thinning is observed in Fig. 1(b).

In Fig. 3(a) exemplary centerline height profiles $h(x,y = 0,t)$ are presented for different times after solid deposition. These profiles were obtained from an analysis of the corresponding interference fringe patterns. The peak height of the rim h_{max} was initially increasing and was determined to reach a maximum value of about $3.75h_0$ in intermediate stages of the experiment. During the course of the experiment the peak is observed to widen over time and in later stages a decrease of the peak height is visible.

In experiments with solid deposition we observe a systematic change in the shape of the rim as it propagates along the rivulet. Initially the rim exhibits a considerable asymmetry in the streamwise direction, which gradually disappears at later times. The

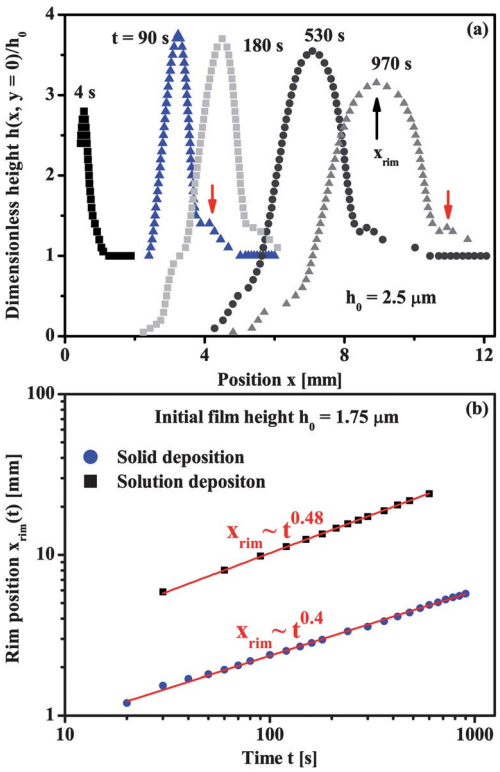

Fig. 3 (a) Exemplary rivulet center height profiles for various times after deposition of a pellet of compressed SDS powder onto a glycerol rivulet of initial film height $h_0 = 2.5$ μm. The peak height reaches a maximum value of $h_{max} \approx 3.75h_0$ and widens at later stages. (b) Exemplary measurements of the rim position as a function of time for solution- (blue triangles) as well as solid deposition (black circles) of SDS. The solid lines correspond to power law fits of the form $x_{rim} \approx t^{\alpha}$ with exponents α of 0.48 and 0.4 for solution and solid deposition, respectively.

asymmetry at early stages manifests itself in the curvature of the interference fringes, which is strong ahead of the peak position while the fringes are practically orthogonal to the flow direction behind the peak, as depicted in Fig. 1(c). As the experiment progresses this asymmetry vanishes as shown in Fig. 1(d). Another phenomenon observed during the spreading process is fingering instabilities,[1,2,16,26,50,54] which typically occur immediately after solid SDS deposition, but in the later stages in the case of solution deposition as shown in Fig. 4.

Fig. 4 Microscope image of fingering instability observed after solution deposition for $h_0 = 1.63$ μm, $w = 1.5$ mm and $t = 542$ s.

Fig. 3(b) shows typical measurements of the rim position as a function of time $x_{rim}(t)$ for solution- (black squares) as well as solid deposition (blue circles). In both cases the experimental data can, to very good approximation, be represented by a power law relation $x_{rim} \approx t^{\alpha}$. The solid lines in Fig. 3(b) correspond to power law fits with exponents α of 0.48 and 0.4 for solution- and solid deposition, respectively. Results for solution deposition vary notably from the ones for solid deposition. The difference can most likely be attributed to the flow induced by the spreading of the deposited droplet as opposed to the case of solid deposition where the source of surfactant can be considered immobile. This difference results in an increase in the observed propagation rate of the surfactant front for solution deposition as illustrated in Fig. 3(b).

In Fig. 5(a) we present fitted power law exponents α for various aspect ratios $\varepsilon = 2h_0/w$. Experimental exponents were obtained for rivulet widths of $w = 1.5$ mm and $w = 0.3$ mm as indicated in by solid symbols. Since interference microscopy is limited to film thicknesses below approximately 10 μm, the smaller rivulet width w allowed the application of this method for higher aspect ratios.

Fig. 5(b) shows the rim position $x_{rim}(t = 1000\ \text{s})$ after solid deposition as a function of the initial film thickness for $w = 1.5$ mm. Filled symbols represent experimental data. The solid line in Fig. 5(b) corresponds to a power law relation $x_{rim}(1000\ \text{s}) \sim \sqrt{h_0}$, which is an excellent approximation to the experimentally measured results. The same scaling with h_0 had been observed for the case of insoluble surfactants.[3,45,46]

Fig. 6(a) shows the spreading exponent α for the case of solution deposition, as a function of the surfactant concentration in the deposited droplet. The exponent appears to be independent of the surfactant concentration with an average value of $\langle\alpha\rangle = 0.42$. Merely for the highest of the investigated concentrations of $c = 0.044$ mol l^{-1}, a slight decrease in the spreading exponent is noticeable. We observed that the SDS solution with concentration of $c = 0.044$ mol l^{-1} became turbid and gel-like and its viscosity increased significantly as compared to solutions with lower concentration. We argue that a corresponding local increase in viscosity retards the spreading dynamics of the deposited solution droplet, such that the experiment resembles more the case of solid SDS deposition. Consistent with this notion, a reduction of the measured spreading exponent towards the average value shown in Fig. 5 for solid deposition is observed.

Fig. 6(b) shows the spreading exponent α measured for different initial film heights h_0 and deposited droplets with a surfactant concentration of $c = 0.044$ mol l^{-1}, consistent with the results in Fig. 5. The spreading exponent is to good approximation independent of the film thickness within the considered range with an average value of $\langle\alpha\rangle = 0.42$.

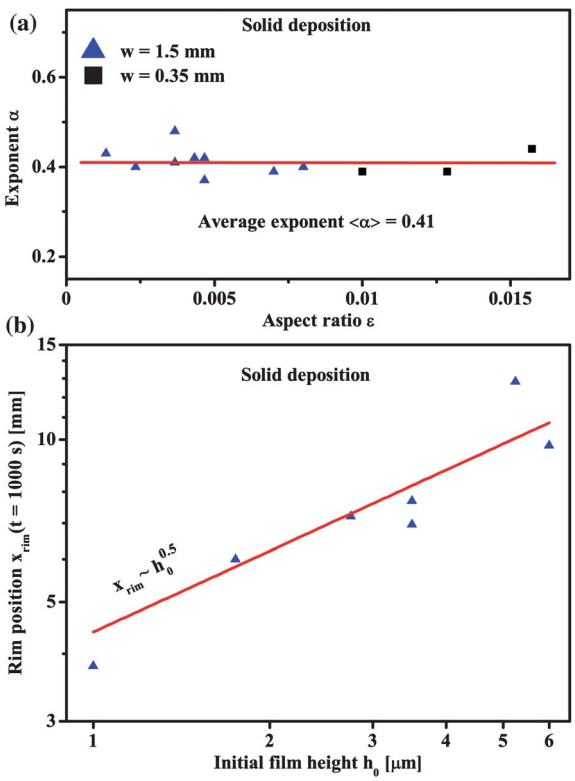

Fig. 5 (a) Spreading exponents α for solid deposition as a function of the aspect ratio ε for rivulet widths of $w = 1.5$ mm (blue triangles) and $w = 0.3$ mm (black squares). (b) Rim position $x_{rim}(t = 1000\ \text{s})$ as a function of h_0 after solid deposition onto rivulets of width $w = 1.5$ mm. Experimentally obtained values are indicated by symbols, the scaling relation $x_{rim}(1000\ \text{s}) \sim \sqrt{h_0}$ is indicated by the red solid line.

IV. The mathematical model for soluble surfactant spreading

A. Thin films – the lubrication model with vertical averaging

We consider the spreading of a soluble surfactant on a thin liquid film of constant Newtonian viscosity that is chemically confined to a hydrophilic strip of width w and length L. The model geometry is illustrated in Fig. 7. Since the lateral aspect ratio $\varepsilon \equiv 2h_0/w \ll 1$, the small-slope approximation can be applied to derive an evolution equation for the sub-phase height profile[38] that accounts for the influence of Marangoni stresses, hydrostatic and capillary pressure gradients. An equation for surfactant surface

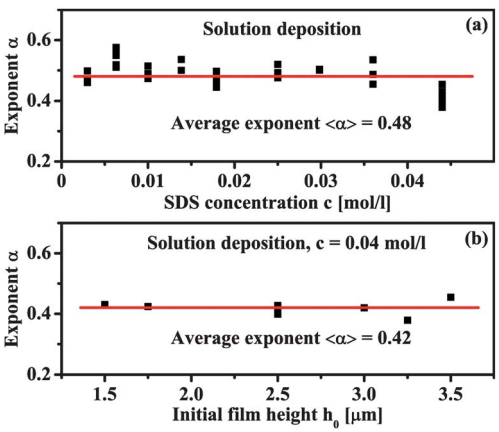

Fig. 6 (a) Fitted spreading exponents for various concentrations of deposited SDS solution for initial liquid film heights in the range of 1.5 μm $\leq h_0 \leq$ 4.5 μm. (b) Fitted spreading exponents as a function of initial liquid film height for the concentration $c_0 = 0.044$ mol l^{-1} of the deposited SDS solution.

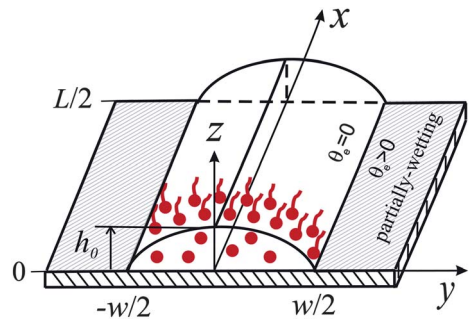

Fig. 7 Sketch of the rivulet geometry with initial surfactant distribution.

transport including the effects of convection by the liquid surface motion as well as surface diffusion has been derived in ref. 7 and 51. In the case of soluble surfactants an additional term appears in this equation that accounts for bulk–surface exchange due to adsorption–desorption processes. Jensen and Grotberg developed a theoretical model for the dynamics of thin liquid films in the presence of non-uniform distributions of a soluble surfactant.[24] The authors assumed a linear equation of state $\gamma = \gamma_0 - A\Gamma$ with a positive constant A as well as a linear relation between the surfactant bulk concentration in the liquid film $c(x,y,z,t)$ and the equilibrium surface concentration Γ_{eq}. The bulk transport of surfactant is governed by the convection and diffusion equation

$$\frac{\partial c}{\partial t} + \boldsymbol{u}\cdot\nabla c = D_b \nabla^2 c, \tag{1}$$

where D_b is the bulk diffusion coefficient.

We have generalized this model as to include the full non-linear Langmuir equation for bulk–surface exchange J as well as the corresponding equilibrium isotherm

$$J = k_1 c_s\left(1 - \frac{\Gamma}{\Gamma_\infty}\right) - k_2\Gamma \tag{2}$$

$$\frac{\Gamma_{eq}}{\Gamma_\infty} = \frac{k_1 c_s}{k_2\Gamma_\infty + k_1 c_s} \tag{3}$$

where J is the surfactant flux with units of mol m^{-2} s^{-1}, $k_{1,2}$ are the adsorption- and desorption rate constants, Γ_∞ is the maximum surface concentration at complete coverage of the surface, and $c_s(x,y,t) = c(x,y,z = h,t)$ is the bulk concentration at the surface.

For thin films and fast vertical diffusion the concentration $c(x,y,z,t)$ can be decomposed into a component independent of z and a small fluctuation[24]

$$c = C(x,y,t) + \varepsilon^2 \mathrm{Pe}_b C_1(x,y,z,t), \tag{4}$$

where Pe_b is the bulk Peclet number defined in eqn (15) and

$$\frac{1}{h}\int_0^h C_1(x,y,z,t)\mathrm{d}z = 0. \tag{5}$$

Averaging eqn (1) with respect to z, one arrives at a convection–diffusion equation for the height-averaged bulk concentration $C(x,y,t)$, which is discussed below.

The non-linear equation of state derived from the Gibbs adsorption isotherm follows as

$$\gamma = \gamma_0 + RT\Gamma_\infty \ln\left(1 - \frac{\Gamma}{\Gamma_\infty}\right) \tag{6}$$

where R is the universal gas constant and T the absolute temperature. We used eqn (6) and (3) to fit the experimental data in Fig. 2 for the dependence of surface tension on bulk concentration, $\gamma(C)$, which yielded the parameter values $\Gamma_\infty = 4.2 \times 10^{-6}$ mol m^{-2} and $k_2/k_1 = 1.7 \times 10^6$ m^{-1}. Since we do not take into account the presence of surfactant micelles, the validity of this model is restricted to concentrations below the critical micelle concentration. We introduce the scaled variables

$$\overline{x} \equiv \frac{2x}{w}, \quad \overline{y} \equiv \frac{2y}{w}, \quad \overline{h} \equiv \frac{h}{h_0}, \quad \overline{t} \equiv \frac{t}{t_M} \equiv t\,\frac{4h_0\Delta\gamma_m}{\mu w^2} \tag{7}$$

$$\overline{p} \equiv \frac{pw^2}{4h_0\Delta\gamma_m}, \quad \overline{\Gamma} \equiv \frac{\Gamma}{\Gamma_\infty}, \quad \overline{C} \equiv \frac{k_1 C}{k_2\Gamma_\infty}. \tag{8}$$

and arrive at the dimensionless system of equations[7,24,38,51,57]

$$\frac{\partial\overline{h}}{\partial\overline{t}} + \overline{\nabla}\left[\frac{1}{2}\left(\overline{h}^2\overline{\nabla}\overline{\gamma}\right) - \frac{\varepsilon^2}{3}\overline{h}^3\overline{\nabla}\overline{p}\right] = 0 \tag{9}$$

$$\frac{\partial\overline{\Gamma}}{\partial\overline{t}} + \overline{\nabla}\left[\overline{h}\,\overline{\Gamma}\,\overline{\nabla}\overline{\gamma} - \frac{\varepsilon^2}{2}\overline{h}^2\overline{\Gamma}\,\overline{\nabla}\overline{p} - \frac{1}{\mathrm{Pe}_s}\overline{\nabla}\,\overline{\Gamma}\right] = K\left(\overline{C}\left(1-\overline{\Gamma}\right) - \overline{\Gamma}\right) \tag{10}$$

$$\frac{\partial\overline{C}}{\partial\overline{t}} + \left[\frac{\overline{h}}{2}\overline{\nabla}\overline{\gamma} - \frac{\varepsilon^2}{3}\overline{h}^2\overline{\nabla}\overline{p}\right]\overline{\nabla}\,\overline{C} - \frac{1}{\mathrm{Pe}_b\overline{h}}\overline{\nabla}\left[\overline{h}\overline{\nabla}\,\overline{C}\right] = \frac{\beta K}{\overline{h}}\left(\overline{\Gamma} - \overline{C}\left(1-\overline{\Gamma}\right)\right) \tag{11}$$

$$\bar{p} = -\bar{\gamma}\bar{\nabla}^2\bar{h} + \mathrm{Bo}\bar{h} + \bar{\Pi} \tag{12}$$

$$\overline{\gamma} = \frac{1}{\Delta\gamma_m}\left(\gamma_0 + RT\Gamma_\infty\ln\left(1-\overline{\Gamma}\right)\right), \tag{13}$$

where the following dimensionless parameters are introduced

$$\varepsilon \equiv \frac{2h_0}{w}, \quad \mathrm{Bo} \equiv \frac{\rho g w^2}{4\Delta\gamma_m}, \quad \mathrm{Pe}_s \equiv \frac{h_0\Delta\gamma_m}{\mu D_s}, \tag{14}$$

$$\mathrm{Pe}_b \equiv \frac{h_0\Delta\gamma_m}{\mu D_b}, \quad \beta \equiv \frac{k_1}{k_2 h_0}, \quad K \equiv k_2 t_M \tag{15}$$

Here, p is the augmented pressure,[38] Π is the disjoining pressure contribution that is relevant for ultrathin films,[9] Bo is the Bond number, Pe_s and Pe_b are the Peclet numbers for surfactant surface and bulk transport, D_s is the surface diffusion coefficient, $\Delta\gamma_m$ is the maximum spreading pressure as indicated in Fig. 2, K is the ratio of the time scale of the flow and the time scale of desorption, and β is the surface–bulk partitioning parameter proportional to the ratio of adsorption–desorption rate constants.[59]

In the following subsections, we present two separate sets of initial and boundary conditions (BCs), termed finite and continuous surfactant supply, that represent solution- and solid deposition, respectively, as used in the experiments.

1. Initial and boundary conditions for continuous surfactant supply – a representation of solid deposition. The deposition of solid SDS is represented in our model by a continuous supply of

surfactant. A certain initial quantity of surfactant is distributed uniformly in the region $0 \le x \le \bar{x}_0$. We consider two cases with respect to the length of the surfactant deposition region x_0: an area source with $\bar{x}_0 = 1$ and a line source with $\bar{x}_0 = 0$. We define the initial surface and bulk concentrations

$$\bar{\Gamma}(\bar{x},0) = b\bar{\Gamma}_0(1 - \tan h[B(\bar{x} - \bar{x}_0)]), \quad (16)$$

$$\bar{C}(\bar{x},0) = b\bar{C}_0(1 - \tan h[B(\bar{x} - \bar{x}_0)]). \quad (17)$$

The parameter $B \equiv 20$ defines the steepness of the initial concentration curve. The initial concentrations $\bar{\Gamma}_0$ and $\bar{C}_0$ are assumed to be in equilibrium and thus are related through eqn (3) as

$$\bar{C}_0(\bar{x},\bar{t} = 0) = \bar{\Gamma}(\bar{x},\bar{t} = 0)/(1 - \bar{\Gamma}(\bar{x},\bar{t} = 0)). \quad (18)$$

For the case of $\bar{x}_0 = 1$ (area source), we impose constant surface and bulk concentrations in the region $0 \le \bar{x} \le \bar{x}_0$

$$\bar{\Gamma}(\bar{x} \le \bar{x}_0,\bar{y},\bar{t}) = \bar{\Gamma}_0,\ \bar{C}(\bar{x} \le \bar{x}_0,\bar{y},\bar{t}) = \bar{C}_0, \quad (19)$$

and choose $b = 1/2$.

For the case of $\bar{x}_0 = 0$ (line source), we impose constant surface and bulk concentrations at the boundary $\bar{x} = 0$,

$$\bar{\Gamma}(\bar{x} = 0,\bar{y},\bar{t}) = \bar{\Gamma}_0,\ \bar{C}(\bar{x} = 0,\bar{y},\bar{t}) = \bar{C}_0, \quad (20)$$

and set $b = 1$, which corresponds to a smooth transition from finite to vanishing concentration values.

The system of eqn (9)–(13) is solved together with the following boundary conditions (BCs)

$$\frac{\partial \overline{h}}{\partial \overline{x}}(0,\overline{y}) = \frac{\partial \overline{p}}{\partial \overline{x}}(0,\overline{y}) = 0 \quad (21)$$

$$\frac{\partial \overline{h}}{\partial \overline{y}}(\overline{x},0) = \frac{\partial \overline{\Gamma}}{\partial \overline{y}}(\overline{x},0) = \frac{\partial \overline{C}}{\partial \overline{y}}(\overline{x},0) = \frac{\partial \overline{p}}{\partial \overline{y}}(\overline{x},0) = 0 \quad (22)$$

$$\overline{\Gamma}\left(\frac{L}{2},\overline{y}\right) = \overline{C}\left(\frac{L}{2},\overline{y}\right) = \frac{\partial \overline{p}}{\partial \overline{x}}\left(\frac{L}{2},\overline{y}\right) = 0 \quad (23)$$

$$\overline{h}\left(\frac{L}{2},\overline{y}\right) = \overline{f}(\overline{y}), \quad (24)$$

where $\bar{f}(\bar{y})$ is the boundary height profile corresponding to a glycerol rivulet in static equilibrium without surfactants adsorbed. If the influence of gravity is negligible, this profile is parabolic $\bar{f}(\bar{y}) = 1 - \bar{y}^2$. Eqn (21) and (22) reflect the mirror symmetry of the system with respect to the planes $\bar{x} = 0$ and $\bar{y} = 0$. Boundary conditions (eqn (23) and (24)) represent a clean, uncontaminated liquid surface at a large distance from the surfactant deposition region.

The chemical patterning is implemented by means of a discontinuous disjoining pressure, which is represented by the term $\bar{\Pi}$ in eqn (12). On the hydrophilic strip $0 < \bar{y} < 1$, where glycerol is deposited, we include a repulsive disjoining pressure representing non-retarded van der Waals forces[22]

$$\Pi_i = A/h^3 \quad (25)$$

where $A > 0$ is the Hamaker constant.

Since in our experiments the rivulet volume was sufficiently low such that the liquid remained confined to the hydrophilic region, we only include a narrow partially wetting strip $1 < \bar{y} < 1.05$ adjacent to the hydrophilic strip in our model. In this region, we use the two-term disjoining pressure model introduced in ref. 42:

$$\Pi_0 = E\left[\left(\frac{h_*}{h}\right)^n - \left(\frac{h_*}{h}\right)^m\right], \quad (26)$$

where h_* is the constant thickness of an ultrathin precursor layer, $n > m > 1$ are integers,

$$E \equiv \frac{(n-1)(m-1)}{h_*(n-m)}\gamma(1 - \cos\theta_e) \quad (27)$$

and θ_e the equilibrium contact angle. After non-dimensionalization, we obtain the expressions

$$\bar{\Pi}_i = -\bar{A}/\bar{h}^3 \text{ for } 0 < \bar{y} < 1 \quad (28)$$

$$\overline{\Pi}_0 = \overline{E}\left[\left(\frac{\overline{h}_*}{\overline{h}}\right)^n - \left(\frac{\overline{h}_*}{\overline{h}}\right)^m\right] \quad \text{for } 1 < \overline{y} < 1.05, \quad (29)$$

where

$$\overline{A} \equiv \frac{A}{\Delta\gamma_m \varepsilon^2 {h_0}^2} \quad (30)$$

$$\overline{E} \equiv \overline{\gamma}\,\frac{w^2(n-1)(m-1)}{{h_0}^2\,\overline{h}_*(n-m)}(1 - \cos\theta_e) \quad (31)$$

In our simulations we use the following values: $\bar{h}_* = 0.005$, $\theta_e = 10°$, $n = 3$, $m = 2$ and $A = 7 \times 10^{-20}$ N m.

The BCs at the outer boundary of the partially wetting strip are represented by the no-flux conditions

$$\frac{\partial \overline{h}}{\partial \overline{y}}(\overline{x},1.05,\overline{t}) = 0 = \frac{\partial \overline{p}}{\partial \overline{y}}(\overline{x},1.05,\overline{t}) \quad (32)$$

$$\frac{\partial \overline{\Gamma}}{\partial \overline{y}}(\overline{x},1.05,\overline{t}) = 0 = \frac{\partial \overline{C}}{\partial \overline{y}}(\overline{x},1.05,\overline{t}) \quad (33)$$

The initial conditions for the film thickness in the partially and completely wetting regions are prescribed to be $\bar{h} = \bar{h}_*$ and $\bar{h}(\bar{x},\bar{y},0) = \bar{h}_* + \bar{f}(\bar{y})$, respectively.

2. Initial and boundary conditions for finite surfactant supply – a representation of solution deposition. The deposition of a droplet of an SDS–glycerol solution onto a liquid rivulet is represented in our model by finite surfactant supply. A limited initial quantity of surfactant is distributed uniformly in the region $0 \le x \le \bar{x}_0$, reflected by the initial conditions for surface concentration

$$\overline{\Gamma}(\overline{x},0) = \frac{\overline{\Gamma}_0}{2}\left(1 - \tan h\left[B(\overline{x} - \overline{x}_0)\right]\right), \quad (34)$$

and bulk concentrations

$$\overline{C}(\overline{x},0) = \frac{\overline{C}_0}{2}\left(1 - \tan h\left[B(\overline{x} - \overline{x}_0)\right]\right), \quad (35)$$

which subsequently depletes during the spreading process.

ART ■ C2SM25484K

In the experiments, the height of the deposited surfactant drop was up to 10 times the center height of the rivulet. Consequently, we accounted for the presence of the droplet in the initial height profile, as sketched in Fig. 9(b),

$$\bar{h}(\bar{x} \le \bar{x}_0,\bar{y},0) = \bar{f}(\bar{y}) + \bar{h}_{\mathrm{drop}}\bar{f}(\bar{y})(\bar{x}_0{}^2 - \bar{x}^2) \tag{36}$$

$$\bar{h}(\bar{x} > \bar{x}_0,\bar{y},0) = \bar{f}(\bar{y}), \tag{37}$$

where the parameter $\bar{h}_{\mathrm{drop}}$ was varied between 0 and 10. Because of the spreading of the droplet, extreme film thinning – as observed for solid deposition – does not occur and disjoining pressure effects need not to be considered. Consequently, eqn (32) and (33) were replaced with

$$\bar{h}(\bar{x},1,\bar{t}) = 0 \tag{38}$$

$$\frac{\partial \overline{\Gamma}}{\partial \bar{y}}(\bar{x},1,\bar{t}) = 0 = \frac{\partial \overline{C}}{\partial \bar{y}}(\bar{x},1,\bar{t}). \tag{39}$$

The applicable BCs at $\bar{x} = 0$ are

$$\frac{\partial \overline{\Gamma}}{\partial \bar{x}}(0,\bar{y}) = \frac{\partial \overline{C}}{\partial \bar{x}}(0,\bar{y}) = 0. \tag{40}$$

The remaining BCs given in eqn (21)–(24) remain valid.

B. Surfactant spreading simulations using the ALE method

The assumption of fast vertical diffusion

$$\frac{t_{\mathrm{d}}}{t_{\mathrm{M}}} \equiv \frac{h_0{}^2}{D_{\mathrm{b}}}\frac{4h_0\Delta\gamma_{\mathrm{m}}}{\mu w^2} = \varepsilon^2 \cdot \mathrm{Pe}_{\mathrm{b}} \ll 1 \tag{41}$$

is only valid for sufficiently thin films and large diffusion coefficients, such that the bulk concentration is to good approximation independent of the vertical coordinate z. In the case of soluble surfactants, the rim height can be up to 4 times the initial rivulet height, such that this assumption may not be automatically fulfilled in the rim region. To evaluate the consequences of vertical concentration non-uniformities, we model surfactant spreading without utilizing the lubrication approximation.

We implement the deformability of the computational domain using the Arbitrary Lagrangian–Eulerian (ALE) method. This approach allows for a time-dependant mesh that is suitable for solving problems with moving interfaces. We implemented a two-dimensional model for surfactant spreading at the liquid–air interface using this method, since computational costs of three-dimensional ALE calculations are too high given the small aspect ratio of our systems. The flow of the liquid sub-phase is modeled with the full Navier–Stokes equations. The surfactant bulk concentration evolves according to the convection and diffusion eqn (1). Surface transport of the surfactant adsorbed at the liquid–air interface is described by

$$\frac{\partial \Gamma}{\partial t} + \nabla_{\mathrm{s}}\cdot(\Gamma\mathbf{u}) = D\nabla_{\mathrm{s}}{}^2\Gamma + k_1 c_{\mathrm{s}} - k_2\Gamma \tag{42}$$

where $c_{\mathrm{s}}(x) = c(z = h(x))$ is the bulk concentration evaluated at the surface. Eqn (42) is reformulated for a one-dimensional domain $\zeta \in \left[0,\frac{L}{2}\right]$, which represents the interface *via* the parametrization

$$x = \zeta,\ z = h(\zeta) \tag{43}$$

with the outward unit normal vector

$$\boldsymbol{n} = \frac{1}{H}\left(-\frac{\partial h}{\partial \zeta},1\right), \quad \text{where } H \equiv \sqrt{1 + \left(\frac{\partial h}{\partial \zeta}\right)^2}. \tag{44}$$

Thus, we derive the one-dimensional evolution equation in the limit of vanishing surface diffusion

$$k_1 c_{\mathrm{s}} - k_2\Gamma = \frac{1}{H^2}\left[u_x\frac{\partial \Gamma}{\partial \zeta} + \Gamma\left(\frac{\partial u_x}{\partial x} + \frac{\partial h}{\partial \zeta}\frac{\partial u_x}{\partial z}\right)\right] + \frac{1}{H^2}\frac{\partial h}{\partial \zeta}\left[u_z\frac{\partial \Gamma}{\partial \zeta} + \Gamma\left(\frac{\partial u_z}{\partial x} + \frac{\partial h}{\partial \zeta}\frac{\partial u_z}{\partial z}\right)\right] + \frac{\partial \Gamma}{\partial t}. \tag{45}$$

The BCs for the Navier–Stokes equation are

$$u_x(z=0) = 0 = u_z(z=0) \tag{46}$$

$$u_x(x=0) = 0 = u_x\left(x = \frac{L}{2}\right) \tag{47}$$

$$\frac{\partial u_z}{\partial x}(x=0) = 0 = \frac{\partial u_z}{\partial x}\left(x = \frac{L}{2}\right) \tag{48}$$

representing no-slip and no-penetration at the solid–liquid interface as well as no flux or symmetry at the lateral domain boundaries. In addition, surface tension gradients at the interface are taken into account *via* the weak form boundary condition[40]

$$\int \boldsymbol{w}\cdot\underline{\underline{\sigma}}\cdot\boldsymbol{n}\mathrm{d}s = \int \gamma\nabla_{\mathrm{s}}\cdot\boldsymbol{w}\mathrm{d}s\,, \tag{49}$$

where γ is the surface tension, $\boldsymbol{w}$ denotes a test function, and $\underline{\underline{\sigma}}$ is the stress tensor.

The BCs for the surfactant surface and bulk concentrations are

$$\frac{\partial c}{\partial z}(z=0) = 0 \tag{50}$$

$$-D_{\mathrm{b}}(\boldsymbol{n}\cdot\nabla c) = k_1 c_{\mathrm{s}} - k_2\Gamma \text{ at } z = h \tag{51}$$

$$\frac{\partial c}{\partial x}(x=0) = 0 = \frac{\partial c}{\partial x}\left(x = \frac{L}{2}\right) \tag{52}$$

$$\frac{\partial \Gamma}{\partial \zeta}(\zeta=0) = 0 = \frac{\partial \Gamma}{\partial \zeta}\left(\zeta = \frac{L}{2}\right). \tag{53}$$

Eqn (50) indicates that the surfactant does not adsorb at the solid–liquid interface. Eqn (52) and (53) are no-flux or symmetry conditions at the lateral domain boundaries. Eqn (51) describes bulk–surface exchange.

V. Numerical results

A. Finite surfactant supply representing solution deposition

In the case of finite surfactant supply, the surfactant depletes at the deposition region as time progresses and redistributes along the rivulet surface and into the sub-phase, whereby the total surfactant amount

$$\int_0^{\frac{L}{2}}\int_{-\frac{w}{2}}^{\frac{w}{2}}\left(\Gamma+\int_0^h C\mathrm{d}z\right)\mathrm{d}x\mathrm{d}y=\int_0^{\frac{L}{2}}\int_{-\frac{w}{2}}^{\frac{w}{2}}(\Gamma+hC)\mathrm{d}x\mathrm{d}y \qquad (54)$$

is conserved. In Fig. 8(a) and (b) we present typical examples for the time evolution of the height profile $\bar{h}(\bar{x},\bar{y}=0,\bar{t})$ and surfactant bulk concentration $\bar{C}(\bar{x},\bar{y}=0,\bar{t})$ at the rivulet center line for, $\bar{C}_0 = 1.4$ and $\bar{h}_{\mathrm{drop}} = 0$. The formation of a propagating rim and a crater near the deposition area is qualitatively similar to insoluble surfactant spreading.[45,46]

The time evolution of the rim position $\bar{x}_{\mathrm{rim}}$ is presented in Fig. 9(a). Within certain time intervals, the rim position $\bar{x}_{\mathrm{rim}}(t)$ is well approximated by a power law $\bar{x}_{\mathrm{rim}} \approx \bar{t}^{\alpha}$. The spreading exponents α extracted from the data presented in Fig. 9(a) fall in the range 0.35–0.47, depending on the aspect ratio ε and the time interval for which a power law relation was fitted. For sufficiently large $\bar{h}_{\mathrm{drop}}$, the numerically obtained spreading exponents are in excellent agreement with the experimental value of around 0.48 for solution deposition. Moreover, we found that the spreading exponent is independent of the initial concentration $\bar{C}_0$, consistent with the results of Fig. 6(a).

The solid lines in Fig. 9(c) represent the time evolution of the rim height $\bar{h}_{\mathrm{max}}(\bar{t})$ for different values of $\bar{h}_{\mathrm{drop}}$. The rapid increase of $\bar{h}_{\mathrm{max}}(\bar{t})$ for $\bar{t} \lesssim 2$ represents the rim formation in the early stage of the spreading process. Several local maxima in $\bar{h}_{\mathrm{max}}(\bar{t})$ are

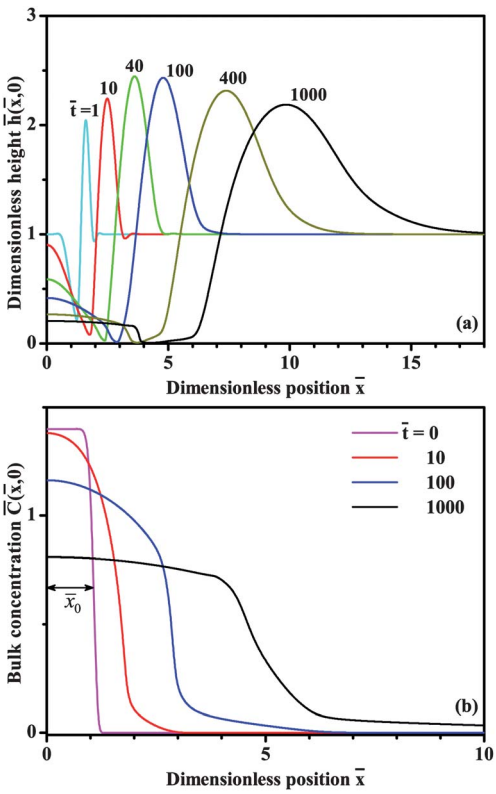

Fig. 8 Time evolution of (a) the centerline height profile $\bar{h}(\bar{x},\bar{y}=0,\bar{t})$ and (b) the dimensionless surfactant bulk concentration $\bar{C}(\bar{x},\bar{y}=0,\bar{t})$ for the parameters settings $\bar{x}_0 = 1$, $\varepsilon = 0.01$, $h_0 = 10$ μm, $\bar{h}_{\mathrm{drop}} = 0$, $\bar{C}_0 = 1.4$, $K = 1000$, $\beta = 0.06$, $\mathrm{Pe_s} = 1000$, $\mathrm{Pe_b} = 100$, and $\mathrm{Bo} = 0$.

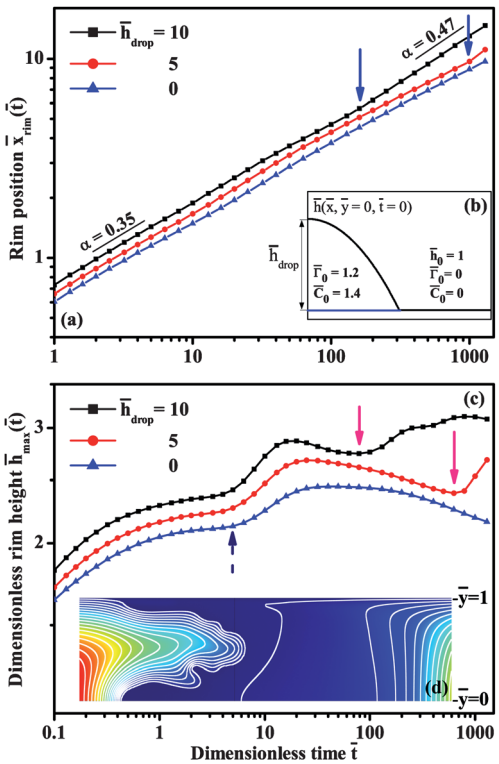

Fig. 9 (a) Rim position $\bar{x}_{\mathrm{rim}}(\bar{t})$ for different drop heights with parameter values $\bar{x}_0 = 1$, $\mathrm{Pe_s} = 1000$, $\varepsilon = 0.01$, $\mathrm{Bo} = 0$. (b) Initial conditions of the centerline height profile $\bar{h}(\bar{x},\bar{t}=0)$ and the surface- and bulk concentrations for different values of $\bar{h}_{\mathrm{drop}}$. (c) Maximum height *vs.* dimensionless time for rivulets with finite surfactant supply for different values of surfactant drop height with $\bar{x}_0 = 1$, $\varepsilon = 0.01$, $h_0 = 10$ μm, $\bar{C}_0 = 1.4$, $K = 1000$, $\beta = 0.06$, $\mathrm{Pe_s} = 1000$, $\mathrm{Pe_b} = 100$, $\mathrm{Bo} = 0$. (d) Fingering instability observed for $\bar{h}_{\mathrm{drop}} = 5$ at $\bar{t} = 790$.

observed. As in the case of insoluble surfactant,[45] the maximum around $\bar{t} = 20$ is due to the decay of transverse surface tension gradients.

Fig. 9(d) illustrates the occurrence of a fingering instability for $\bar{h}_{\mathrm{drop}} = 5$ at time $\bar{t} = 790$. The general morphology and the formation of two main fingers are in good qualitative agreement with the experimental observation in Fig. 4. The time $\bar{t} = 790$ for $\bar{h}_{\mathrm{drop}} = 5$ coincides with the onset of the late-stage increase of $\bar{h}_{\mathrm{max}}$ as indicated with the downward-oriented arrow in Fig. 9(c) for the curve with red circles. We therefore conclude that the spreading of the deposited droplet and the subsequent finger formation enhance the surfactant transport across the crater region and thereby boost the rim propagation. Larger values of $\bar{h}_{\mathrm{drop}}$ induce larger increases in $\bar{h}_{\mathrm{max}}$, and this increase in the rim height is also observed sooner.

B. Continuous surfactant supply representing solid deposition

Fig. 10 (a) and (b) show the time evolution of the height profile $\bar{h}(\bar{x},\bar{y}=0,\bar{t})$ and surfactant bulk concentration $\bar{C}(\bar{x},\bar{y}=0,\bar{t})$ at the rivulet center line, for parameters $\bar{x}_0 = 1$ and $\bar{C}_0 = 11.2$. In Fig. 11 we present the dimensionless position and the maximum height of the rim for two different cases with values of $\bar{x}_0 = 0$ and 1. The essential difference between these two cases

ART ■ C2SM25484K

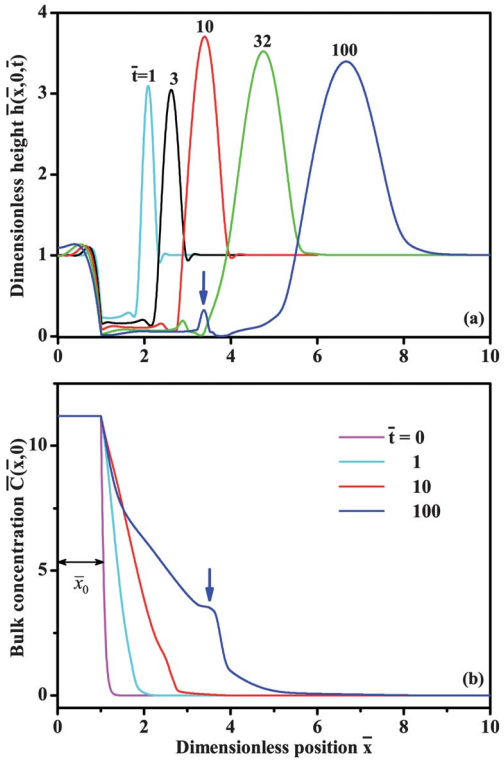

Fig. 10 (a) Evolution of centerline height profile $\bar{h}(\bar{x},\bar{y}=0,\bar{t})$ for continuous surfactant supply. (b) Dimensionless surfactant bulk concentration $\bar{C}(\bar{x},\bar{y}=0,\bar{t})$. All results have been obtained for parameter values $\bar{x}_0 = 1$, $\varepsilon = 0.005$, $h_0 = 10$ μm, $\bar{C}_0 = 11.2$, $\bar{\Gamma}_0 = 0.92$, $K = 1000$, $\beta = 0.06$, $\mathrm{Pe_s} = 1000$, $\mathrm{Pe_b} = 100$, $\mathrm{Bo} = 0$.

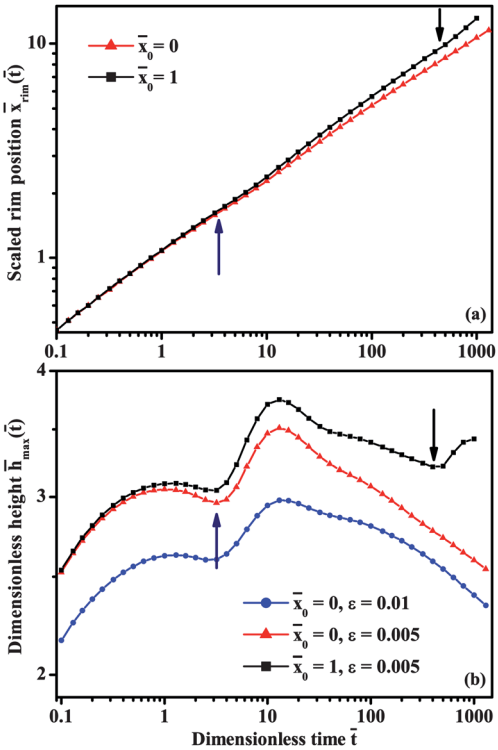

Fig. 11 Dimensionless rim position and maximum height *vs.* dimensionless time for rivulets with continuous supply of soluble surfactant with $h_0 = 10$ μm, $\bar{C}_0 = 11.2$, $\bar{\Gamma}_0 = 0.92$, $K = 1000$, $\beta = 0.06$, $\mathrm{Pe_s} = 1000$, $\mathrm{Pe_b} = 100$, $\mathrm{Bo} = 0$.

is the absence or presence of trapped liquid in the deposition region. In the case of $\bar{x}_0 = 1$ the spreading exponent $\alpha = 0.41$, fitted in the interval $500 < \bar{t} < 1000$, is in excellent agreement with the experimental results in Fig. 5.

The rim height evolution for $\bar{x}_0 = 1$ is qualitatively similar to the case of finite supply. However, the maximum rim height in Fig. 11(b) is significantly larger than in the case of $\bar{h}_{\mathrm{drop}} = 0$ in Fig. 9(c). The crater formation and extreme film thinning close to the perimeter of the surfactant deposition region at $\bar{x} = \bar{x}_0$ temporarily trap the sub-phase liquid in that region.[46] Parts of this trapped liquid are continuously released in the later stages of the spreading process, and undergo a fingering instability as shown in Fig. 12. The rise in the rim height at $\bar{t} = 400$ in the case of $\bar{x}_0 = 1$ [as indicated by the downward-oriented arrow in Fig. 11(b)] is preceded by this expulsion and subsequent finger formation. This process is analogous to the phenomenon described in the previous section for the case of solution deposition, with the temporarily trapped liquid playing the role of the deposited solution droplet.

In the case of $\bar{x}_0 = 0$, the spreading exponent $\alpha = 0.32$, extracted from the results in Fig. 11(a) in the interval $10 < \bar{t} < 1000$, is smaller than both for continuous supply and the case of finite surfactant supply with $\bar{x}_0 = 1$. For $\bar{x}_0 = 0$, extreme thinning in the crater region near $\bar{x} = 0$ effectively cuts off the surfactant supply to the rivulet. As a consequence, no fingering instability occurs and no corresponding increase in the rim height is observed in Fig. 11(b).

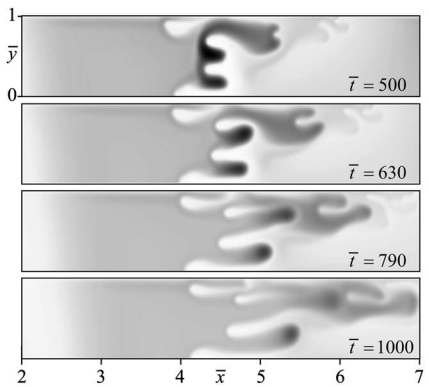

Fig. 12 Numerical simulation of fingering instability for rivulets with continuous supply of soluble surfactant with $\bar{x}_0 = 1$, $\varepsilon = 0.01$, $h_0 = 10$ μm, $\bar{C}_0 = 11.2$, $\bar{\Gamma}_0 = 0.92$, $K = 1000$, $\beta = 0.06$, $\mathrm{Pe_s} = 1000$, $\mathrm{Pe_b} = 100$, $\mathrm{Bo} = 0$.

VI. Discussion

The early stages of the spreading dynamics are influenced by the details of the surfactant deposition procedure in the experiments and by the initial conditions and type of supply used in numerical modeling. Consequently, we focus on the later stages of the spreading dynamics for a comparison between experimental and numerical results. This choice is supported by the fact that exponents extracted from the later stage are found to be in good agreement with the experimental results. Moreover, in experiments a fingering instability is observed almost directly after

ART ■ C2SM25484K

surfactant deposition, while in our simulations the onset of its effect on the rim height and propagation rate occurs relatively late as shown in Fig. 11(b) and 12. Thus, the early onset of the fingering instability in experiments may cause experimental exponents to be larger than numerical ones at early times.

Besides considering spreading exponents, we compare the rim height evolution and its non-monotonic variation. The open symbols in Fig. 13(a) and (b) represent measurements of the time-evolution of the rim height $\bar{h}_{max}$ for two different values of h_0. For $h_0 = 5.6$ μm, a slow increase for $t < 10$ s is observed, followed by a more rapid increase around $t = 20$ s and flattening after $t = 400$ s. For $h_0 = 2.5$ μm, a strong increase in h_{max} is observed for $t < 20$ s, followed by a plateau region with a value of $3.6h_0 \leq h_{max} \leq 3.75h_0$ and a decline of the maximum film height for $t \gtrsim 200$ s.

Since literature data for the sorption rate constants $k_{1,2}$ are not available, we treat the sorption coefficient K as a fit parameter in our model. Jensen and Grotberg reported that rapidly soluble surfactants ($K = 1000$) induce a much higher rim height than surfactants with slow sorption kinetics ($K = 1$) in one-dimensional surfactant spreading, but the comparison was limited to the very early stages of the spreading process.[24] In Fig. 13(a) we also observe that larger K yield higher $\bar{h}_{max}$ in the early stages of surfactant spreading along a rivulet. However, the effect of K diminishes at later times for $t \gtrsim 100$ s.

Thus, for suitably chosen K, the numerical results agree very well with the experimental data in the beginning, as indicated by the solid circles in Fig. 13(a) and (b), but quantitative differences are observed later. The fitted values of K translate into $k_2 = 1.24$ s for $h_0 = 2.5$ μm, and $k_2 = 0.11$ s $h_0 = 5.6$ μm, although k_2 as a material parameter should be independent of h_0. This discrepancy prompted us to find a possible explanation.

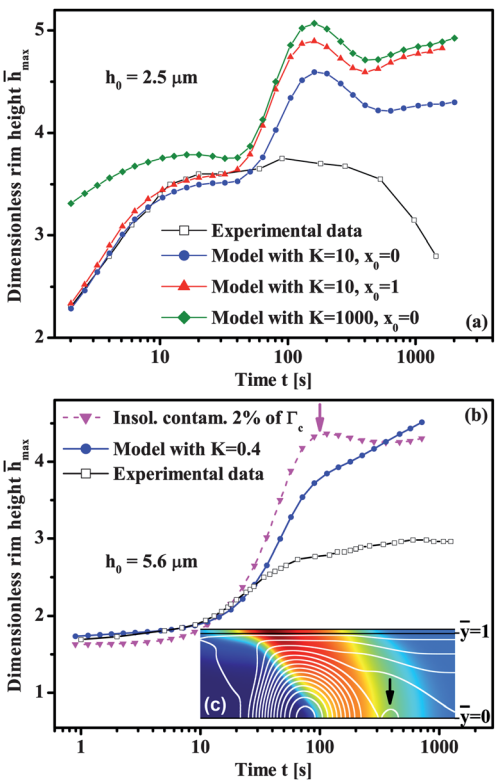

Fig. 13 (a) Measurement and simulations of the temporal evolution of the maximum film height for $h_0 = 2.5$ μm, $w = 1.5$ mm, $\bar{C}_0 = 11.2$, $\bar{x}_0 = 1$, $\beta = 0.11$, $Pe_s = 1000$, $Pe_b = 1000$, $Bo = 1000$. (b) Measurement and simulations of the temporal evolution of the maximum film height for $h_0 = 5.6$ μm, $w = 1.5$ mm, $\bar{C}_0 = 11.2$, $\bar{x}_0 = 0$, $\beta = 0.24$, $K = 10$, $Pe_s = 1000$, $Pe_b = 1000$, $Bo = 0$. (c) False color plot of the insoluble contaminant concentration Γ_{cnt} at $t = 115$ s. The contour lines represent the height profile in the rim region. The parameters used are the same as in (a).

A. Effect of pre-contamination

Since airborne contamination often cannot be avoided during the experiments, Dussaud *et al.*[13] studied the influence of insoluble surface-active contaminants present at the liquid–air interface prior to the surfactant deposition. They found that a low level of pre-contamination has almost no effect on the spreading exponent for an axisymmetric geometry, but causes a noticeable reduction of the rim height.

We implemented pre-contamination in our model as an initially uniform concentration Γ_{cnt}. We assume that the contaminants exhibit the same equations of state as the soluble system SDS–glycerol or the insoluble system oleic acid–glycerol. We consider the following three cases: a contamination level of 1 or 10% of the CMC of SDS–glycerol, or 2% of the surface concentration scale Γ_c as defined in ref. 46 of the insoluble surfactant oleic acid. Results for pre-contaminated surfactant spreading in a 1D Cartesian geometry are presented in Fig. 14. A higher level of contamination lowers the peak value of the rim height at later times, whereby the insoluble contaminant has a stronger effect than the soluble one.

This finding motivated us to inquire whether surface-active contamination could explain the discrepancy between the experimental and numerical results for the rim evolution in Fig. 13. Indeed, the curves depicted with solid circles and triangles indicate that an insoluble pre-contamination slightly lowers the rim height at later stages in Fig. 13(b), but this is preceded by an overshoot in $\bar{h}_{max}$ as marked by the arrow.

Lateral surface tension gradients occur during surfactant spreading on uncontaminated rivulets as a consequence of the non-uniform transverse height profile.[45] Liquid is pushed from

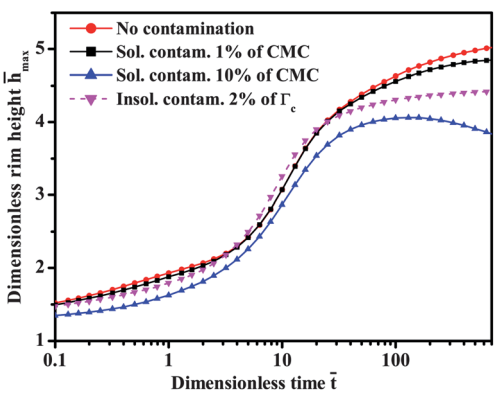

Fig. 14 Rim height evolution $\bar{h}_{max}(\bar{t})$ for surfactant spreading with pre-contamination in a one-dimensional Cartesian geometry for $h_0 = 5.6$ μm, $\bar{C}_0 = 11.2$, $\bar{x}_0 = 0$, $\beta = 0.11$, $Pe_s = 1000$, $Pe_b = 1000$, and $Bo = 0$.

the center of the rivulet to its edges, corresponding to a flattening of the height profile. When an insoluble contaminant is present, the contaminant concentration in the vicinity of the rim is higher near the rivulet edges than in the rivulet center, as illustrated in Fig. 13(c) for an initial insoluble contamination level of $0.02\Gamma_c$. This induces a transverse surface tension gradient that pushes liquid from the edges towards the center of the rivulet and causes the overshoot in Fig. 13(b) marked by the arrow.

A shallow local maximum ahead of rim is observed in Fig. 13(c) as marked by the arrow. This maximum is absent in simulations without contamination, but is frequently observed in experiments, as indicated by the red arrows in Fig. 3(a). Despite this qualitative agreement, we nevertheless conclude that contamination very likely cannot explain the difference between the experimental and numerical rim height profiles in Fig. 13.

B. Effect of non-uniform vertical concentration profiles

To elucidate the influence of non-uniform vertical concentration profiles on the rim height evolution, we performed two-dimensional simulations of surfactant spreading accounting for domain deformability using the ALE method.

Fig. 15 shows the height profile $h(x,t = 10\ \mathrm{s})$ and concentration distribution $c(x,z,t = 10\ \mathrm{s})$ for different values of the bulk diffusion coefficient D_b and finite surfactant supply. A smaller coefficient D_b results in a significantly reduced rim height. Fig. 15(c) shows the bulk concentration profiles at the rim positions $c(x_{rim},z,t = 10\ \mathrm{s})$ for $D_b = 10^{-9}$ and $10^{-11}\ \mathrm{m^2\ s^{-1}}$.

A comparison of the rim height evolution extracted from 2D ALE and 1D lubrication simulations is given in Fig. 15(d). A significant reduction in $\bar{h}_{max}$ is observed for the full ALE solution relative to the lubrication results for $D_b = 10^{-11}\ \mathrm{m^2\ s^{-1}}$.

When the value of D_b is sufficiently large such that the vertical diffusion time scale $t_d = h_0^2/D_b$ is smaller than the Marangoni time scale, the bulk concentration remains essentially uniform in the vertical direction. This allows the surfactant from the interface to effectively desorb into the entire sub-phase film thickness. On the other hand, for small D_b, the bulk concentration has insufficient time to equilibrate, which leads to vertical concentration gradients as shown in Fig. 15(c). Consequently, the bulk concentration at the surface is higher, and the amount of surfactant that is desorbed from the interface is reduced for smaller D_b. This means that for dynamical reasons the surfactant effectively partitions less into the bulk, leading to a smaller rim height.

Assuming uniform vertical concentration profiles, Jensen and Grotberg[24] studied the effect of the surface–bulk partitioning parameter β, which they termed degree of solubility, on the rim height for the two cases of $\beta \to \infty$, an effectively insoluble surfactant, and $\beta = 1$, a 'highly soluble' surfactant. They observed that changing the value of $\beta = 1$ to ∞ induced a significant reduction in the rim height $\bar{h}_{max}$.

In our simulations, the parameter β varies only due to the varying initial height h_0, since the ratio k_1/k_2 is fixed for a specific surfactant. However, we argue that the imbalance in time-scales $t_d > t_M$ in our ALE-based simulations 'dynamically' induces a similar effect as β increases and thus leads to a reduction in the rim height. We thus conclude that accounting for vertical concentration non-uniformities potentially significantly improves the agreement between numerical and experimental rim height profiles in Fig. 13.

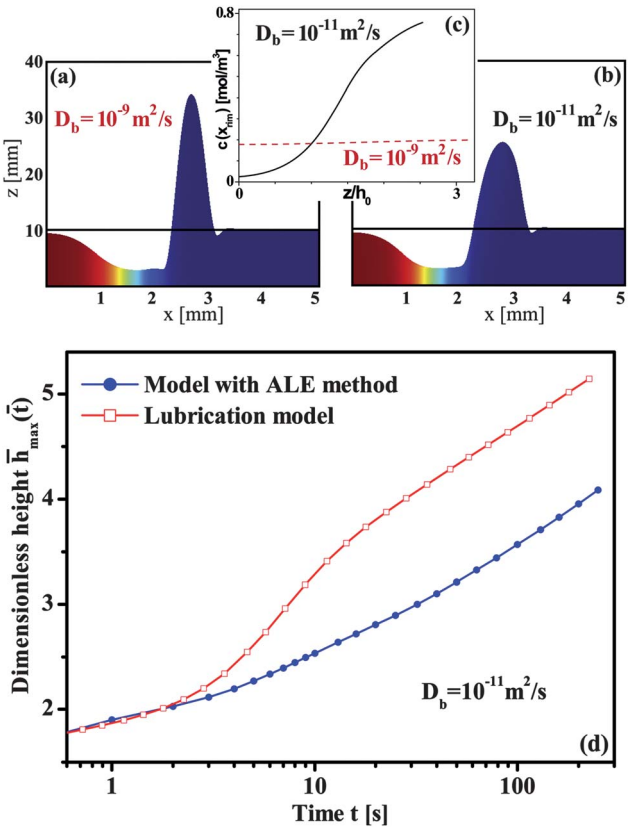

Fig. 15 (a and b) Height profile and concentration distribution (superimposed colors) at $t = 10$ s as extracted from 2D ALE simulations for (a) $D_b = 10^{-9}\ \mathrm{m^2\ s^{-1}}$ and (b) $D_b = 10^{-11}\ \mathrm{m^2\ s^{-1}}$ and parameter settings $h_0 = 10\ \mu\mathrm{m}$, $k_2 = 1.4\ \mathrm{s^{-1}}$ and $k_1 = 8 \times 10^{-7}\ \mathrm{m\ s^{-1}}$. (c) Vertical concentration profile $c(x = x_{rim},z)$ at the rim position at $t = 10$ s extracted from 2D ALE simulations for $D_b = 10^{-9}\ \mathrm{m^2\ s^{-1}}$ and $10^{-11}\ \mathrm{m^2\ s^{-1}}$. (d) Dimensionless rim height $\bar{h}_{max}(\bar{t})$ as extracted from 2D ALE simulations (solid symbols) and 1D simulations using the lubrication approximation (open symbols) for $D_b = 10^{-11}\ \mathrm{m^2\ s^{-1}}$.

VII. Summary and conclusion

We studied the spreading of the soluble surfactant SDS on narrow glycerol rivulets, which were defined by chemical surface patterning of flat and impenetrable Si substrates. We monitored the evolution of the liquid height profile after surfactant deposition at the liquid–air interface both numerically and experimentally using interference microscopy. In our experiments we deposited either small droplets of a surfactant solution in glycerol or a small quantity of solid SDS in the form of compressed powder. The corresponding changes in the initial condition led to significant differences in the spreading behavior.

To complement and rationalize the experimental observations, we developed two different numerical models. The first is based on the lubrication approximation and the assumption of vertically uniform concentration profiles. The second model is based on the full Navier–Stokes equation and convection–diffusion equations for bulk- and surface surfactant transport. It accounts

ART ■ C2SM25484K

for domain deformability and allows for vertically non-uniform concentration profiles.

The most prominent morphological feature of the spreading process is the formation of a local maximum in film thickness and its propagation along the rivulet. Its position can be well approximated by power-laws $x \approx t^{\alpha}$. A proper choice of initial and boundary conditions in the numerical models resulted in spreading exponents that are in excellent agreement with the experimental results. The influence of fingering instabilities, commonly observed during the spreading process, on the rim shape and the propagation rate was discussed. The rim height profiles deduced from experiments were in excellent agreement with numerical simulations based on the lubrication approximation at early times, but systematically lower at later stages. The origin of this discrepancy was identified with the help of deformable-domain simulations and resides in vertical concentration non-uniformities in the rim region that are not accounted for in the lubrication model.

Acknowledgements

The authors would like to thank Steffen Berg and Axel Makurat from Shell International Exploration and Production (Rijswijk, The Netherlands) for the inspiring collaboration. The authors gratefully acknowledge that this research is supported partially by the Dutch Technology Foundation STW, applied science division of NWO and the Technology Program of the Ministry of Economic Affairs.

Notes and references

1 A. B. Afsar-Siddiqui, P. F. Luckham and O. K. Matar, *Langmuir*, 2003, **19**, 703–708.
2 A. B. Afsar-Siddiqui, P. F. Luckham and O. K. Matar, *Adv. Colloid Interface Sci.*, 2003, **106**, 183–236.
3 J. Ahmad and R. S. Hansen, *J. Colloid Interface Sci.*, 1972, **38**, 601–604.
4 J. W. Barret, R. Nürnberg and M. R. E. Warner, *SIAM J. Numer. Anal.*, 2006, **44**, 1218–1247.
5 S. Berg, *Phys. Fluids*, 2009, **21**, 032105.
6 M. R. Booty and M. Siegel, *J. Comput. Phys.*, 2010, **229**, 3864–3883.
7 M. S. Borgas and J. B. Grotberg, *J. Fluid Mech.*, 1988, **193**, 151–170.
8 J. L. Bull, L. K. Nelson, J. T. Walsh, Jr, M. R. Glücksberg, S. Schürch and J. B. Grotberg, *J. Biomed. Eng.*, 1999, **121**, 89–98.
9 N. V. Churaev, B. V. Derjaguin, and V. M. Muller, *Surface Forces*, Kluwer Academic, 1987.
10 R. V. Craster and O. K. Matar, *Langmuir*, 2007, **23**, 2588–2601.
11 A. A. Darhuber, J. Z. Chen, J. M. Davis and S. M. Troian, *Philos. Trans. R. Soc. London*, 2004, **362**, 1037–1058.
12 S. H. Davis, A. Liu and G. R. Sealy, *J. Fluid Mech.*, 1974, **62**, 737–751.
13 A. D. Dussaud, O. K. Matar and S. M. Troian, *J. Fluid Mech.*, 2005, **544**, 23–51.
14 F. F. Espinosa, A. H. Shapiro, J. J. Fredberg and R. D. Kamm, *J. Appl. Physiol.*, 1993, **75**, 2028–2039.
15 P. L. Evans, L. W. Schwartz and R. V. Roy, *J. Colloid Interface Sci.*, 2000, **227**, 191–205.
16 B. J. Fischer and S. M. Troian, *Phys. Fluids*, 2003, **15**, 3837–3845.
17 B. J. Fischer and S. M. Troian, *Phys. Rev. E: Stat., Nonlinear, Soft Matter Phys.*, 2003, **67**, 016309.
18 D. Follows, F. Tiberg, R. K. Thomas and M. Larsson, *Biochim. Biophys. Acta*, 2007, **1768**, 228–235.
19 D. P. Gaver and J. B. Grotberg, *J. Fluid Mech.*, 1990, **213**, 127–148.
20 D. P. Gaver and J. B. Grotberg, *J. Fluid Mech.*, 1992, **235**, 399–414.
21 D. Halpern and J. B. Grotberg, *J. Fluid Mech.*, 1992, **237**, 1–11.
22 J. N. Israelachvili, *Intermolecular and Surface Forces*, Academic Press, San Diego, 2002.
23 A. J. James and J. Lowengrub, *J. Comput. Phys.*, 2004, **201**, 685–722.
24 O. E. Jensen and J. B. Grotberg, *Phys. Fluids A*, 1993, **5**, 58–68.
25 O. E. Jensen, *Phys. Fluids*, 1994, **6**, 1084–1094.
26 O. E. Jensen and S. Naire, *J. Fluid Mech.*, 2006, **554**, 5–24.
27 A. R. Kovscek, H. Wong and C. J. Radke, *AIChE J.*, 1993, **39**, 1072–1085.
28 L. W. Lake, *Enhanced Oil Recovery*, Prentice-Hall, New Jersey, 1989.
29 K. S. Lee and V. M. Starov, *J. Colloid Interface Sci.*, 2007, **314**, 631–642.
30 K. S. Lee and V. M. Starov, *J. Colloid Interface Sci.*, 2009, **329**, 361–365.
31 *CRC Handbook of Chemistry and Physics*, ed. D. Lide, D-240, 1982.
32 C. Lin, C. Hwang, G. Huang and W. Uen, *J. Phys. Soc. Jpn.*, 2002, **71**, 2708–2714.
33 O. K. Matar and S. M. Troian, *Phys. Fluids*, 1998, **10**, 1234–1236.
34 O. K. Matar and S. M. Troian, *Phys. Fluids*, 1999, **11**, 3232–3246.
35 O. K. Matar, *Phys. Fluids*, 2002, **14**, 4216–4234.
36 O. K. Matar and R. V. Craster, *Soft Matter*, 2009, **5**, 3801–3809.
37 A. A. Newman and L. V. Cocks, *Glycerol*, CRC Press, 1968.
38 A. Oron, S. H. Davis and S. G. Bankoff, *Rev. Mod. Phys.*, 1997, **69**, 931–980.
39 K. Piroird, C. Clanetab and D. Quéré, *Soft Matter*, 2011, **7**, 7498–7503.
40 P. H. Saksono and D. Perić, *Comput. Mech.*, 2006, **38**(265), 265–281.
41 L. L. Schramm, *Surfactants: Fundamentals and Applications in the Petroleum Industry*, Cambridge University Press, Cambridge, 2000.
42 L. W. Schwartz and R. R. Eley, *J. Colloid Interface Sci.*, 1998, **202**, 173–188.
43 J. B. Segur and H. E. Oberstar, *Ind. Eng. Chem.*, 1951, **43**, 2117–2120.
44 D. O. Shan and R. S. Schechter, *Improved Oil Recovery by Surfactant and Polymer Flooding*, Academic Press, New York, 1977.
45 D. K. N. Sinz, M. Hanyak, J. Zeegers and A. A. Darhuber, *Phys. Chem. Chem. Phys.*, 2011, **13**, 9768–9777.
46 D. K. N. Sinz, M. Hanyak and A. A. Darhuber, *J. Colloid Interface Sci.*, 2011, **364**, 519–529.
47 R. G. M. van der Sman and S. van der Graaf, *Rheol. Acta*, 2006, **46**, 3–11.
48 V. M. Starov, A. de Ryck and M. G. Velarde, *J. Colloid Interface Sci.*, 1997, **190**, 104–113.
49 K. E. Teigen, P. Song, J. Lowengrub and A. Voigt, *J. Comput. Phys.*, 2011, **230**, 375–393.
50 S. M. Troian, X. L. Wu and S. A. Safran, *Phys. Rev. Lett.*, 1989, **62**, 1496–1499.
51 S. M. Troian, E. Herbolzheimer and S. A. Safran, *Phys. Rev. Lett.*, 1990, **65**, 333–336.
52 W. T. Tsai and L. Y. Liu, *Colloids Surf., A*, 2004, **234**, 51–62.
53 M. R. E. Warner, R. V. Craster and O. K. Matar, *J. Fluid Mech.*, 2004, **510**, 169–200.
54 M. R. E. Warner, R. V. Craster and O. K. Matar, *Phys. Fluids A*, 2004, **16**, 2933–2951.
55 R. M. Weinheimer, D. F. Evans and E. L. Cussler, *J. Colloid Interface Sci.*, 1981, **80**, 357–368.
56 H. A. R. Williams and O. E. Jensen, *J. Biomech. Eng.*, 2000, **122**, 159–166.
57 H. Wong, D. Rumschitzki and C. Maldarelli, *Phys. Fluids*, 1996, **8**, 3203–3204.
58 J.-J. Xu, Z. Li, J. Lowengrub and H. Zhao, *J. Comput. Phys.*, 2006, **212**, 590–616.
59 The total amount of the surfactant in a column of liquid with an infinitesimal base area $dA = dxdy$ is $(Ch + \Gamma)dA$, where the first and second terms correspond to the surfactant amounts in the bulk and at the interface, respectively. If $\bar{C}$ is small, eqn (3) reduces to the linearized Langmuir isotherm $\Gamma \approx k_1 C/k_2$. Thus, $\beta \equiv \frac{k_1}{k_2 h_0}$ is the partitioning ratio of the surfactant amount adsorbed at the surface and dissolved in the bulk liquid. When $\beta \ll 1$ almost all the surfactant is dissolved in the bulk, whereas for $\beta \gg 1$ almost all of it resides at the interface.

Authors Queries

Journal: **SM**

Paper: **c2sm25484k**

Title: **Soluble surfactant spreading on spatially confined thin liquid films**

Editor's queries are marked like this... **1**, and for your convenience line numbers are inserted like this... 5

Query Reference	Query	Remarks
1	For your information: You can cite this article before you receive notification of the page numbers by using the following format: (authors), Soft Matter, (year), DOI: 10.1039/c2sm25484k.	
2	Please carefully check the spelling of all author names. This is important for the correct indexing and future citation of your article. No late corrections can be made.	
3	Do you wish to indicate a corresponding author and/or supply an e-mail address?	
4	Fig. 5a shows '$w = 0.35$ mm', however '$w = 0.3$ mm' is stated in the caption and the text. Would you like to modify the caption or resupply the artwork (preferably as a TIF file at 600 dots per inch)?	
5	Fig. 6b shows '$c = 0.04$ mol l^{-1}', however '$c = 0.044$ mol l^{-1}' is stated in the caption and the text. Would you like to modify the caption or resupply the artwork (preferably as a TIF file at 600 dots per inch)?	
6	Please indicate where ref. 11 should be cited in the text.	